Experimental and Numerical Investigation of Aerodynamic Performance of Airfoils Fitted with Morphing Trailing-edges

Hasan Kamliya Jawahar*, Qing Ai† and Mahdi Azarpeyvand‡
University of Bristol, Bristol, United Kingdom, BS8 1TR

Experimental and numerical studies to characterize the aerodynamic and aeroacoustic performance of a simple NACA 0012 airfoil fitted with various morphing flaps have been successfully carried out. The airfoil was tested with various flap configurations having different camber profiles with a flap deflection angle of $\beta = 10°$. Comprehensive aerodynamic measurements including lift and drag forces, wake flow and pressure distribution over a wide range of angles of attack and chord-based Reynolds numbers were carried out. A detailed Detached Eddy Simulation has been performed for two angles of attack $\alpha = 0°$ and $4°$ and two types of flaps to further investigate the airfoil's flow behaviour and the noise generation mechanism. The experimental and computational results show that the camber profiles of the morphing flaps significantly affect the aerodynamic and aero-acoustic performances. Flow measurements showed that the downstream wake development can also be influenced as a result of changing the flap profile. It was found that highly cambered flap profiles provide higher lift coefficients and increased maximum lift coefficient compared to moderately cambered profiles while the lift-to-drag ratio slightly decreases. Contour plots using iso-surfaces of Q-criterion show that the separation near the trailing-edge is further delayed at high angles of attack for airfoils with highly chambered morphing flap. The far-field noise was calculated using Curle's analogy and it showed an increased noise for highly cambered flap, which corresponds to the increased pressure distribution, turbulence and wall-spectral levels. This study shows that the effective design space of the morphing flaps can be expanded taking into account the optimal aerodynamic performance requirements. The study also suggests that in order to achieve optimum aerodynamic performance, independent surface morphing of the suction and pressure surface camber will be required to delay the onset of flow separation.

Nomenclature

b	=	trailing-edge flap length, m
c	=	airfoil chord length, m
C_L	=	lift coefficient
$C_{L,max}$	=	maximum lift coefficient
C_D	=	drag coefficient
C_p	=	pressure coefficient
D	=	drag force
f	=	frequency, Hz
l	=	airfoil span length, m
L	=	lift force
$L_x \times L_y \times L_z$	=	cell dimensions of computational grid
p_{ref}	=	reference pressure ($= 2 \times 10^{-5}$), Pa
Q	=	second invariant of the velocity-gradient tensor, $1/s^2$
Re_c	=	chord-based Reynolds number
S	=	wing area, m^2
U, U_∞	=	mean velocity, free-stream velocity, m/s
x, y, z	=	streamwise, spanwise and crosswise coordinates, m
y^+	=	dimensionless wall distance
α	=	angle of attack, °
β	=	morphing flap tip deflection angle, °
Φ_{pp}	=	wall-pressure power spectral density, Pa^2/Hz

*PhD Student, Department of Aerospace Engineering, AIAA Student Member, hasan.kj@bristol.ac.uk
†PhD Student, Advanced Composites Centre for Science and Innovation (ACCIS), University of Bristol. Qing.ai@bristol.ac.uk
‡Senior Lecturer and Royal Academy of Engineering Research Fellow, Department of Mechanical Engineering, m.azarpeyvand@bristol.ac.uk

I. Introduction

MORPHING structures have received significant interest from engineering community including the aviation and automobile industries, owing to their potential of high performance, low mechanism complexity and light-weight. Current high-lift systems used on aeroplane wings for example slats, aileron and trailing-edge flaps, mainly consist of discrete rigid structure components which are articulated around hinges and linkages to achieve wing shape change for flow control purposes. As such, the overall system complexity and structure weight are considerably increased. Unlike conventional wing control surfaces, morphing structures for example morphing leading-edge and trailing-edge usually use the conformal structural deformation achieved through bending and twisting of structures to adaptively change wing shape, leading to simplified systems and reduced weight. Furthermore, the intrinsic continuous deformation shape and smooth structure surface in morphing structures significantly reduce airframe noise, particularly the cavity type noise and drags compared to conventional mechanical control surfaces.

Airframe noise is a significant component of aircraft noise during approach to landing. Noise sources including jet noise, landing gear noise and high-lift device noise dominate the acoustic performance of an aircraft. Studies have shown that noise generated by kinetic energy scattering of turbulent eddies in the boundary layer as they cross the wing's trailing-edge becomes dominant for aeroplanes in clean configuration with projected reduction of the high-lift system noise [1]. As such, airfoil self-noise has been considered as an important component of airframe noise during take-off and landing. The airfoil self-noise has also been recognized as a key concern for wind turbine noise [2]. Some of the currently employed passive methods for airfoil trailing-edge noise reduction includes serrated trailing-edges [3–6], porous surface treatments [7–9] and morphing trailing-edges [10]. With the use of morphing surfaces our aim is to address transition delay, separation postponement, lift enhancement, drag reduction, turbulence augmentation and noise suppression [11]. High-lift systems for aircraft wings have been widely used for lift and drag control during take-off and landing and also on wind turbine blades to increase control efficiency of the current yawing and pitching operation systems. However, high-lift devices including slats and flaps have also been identified as significant noise sources while deployed for a high-lift configuration [12]. An ideal method of morphing should achieve the control goal without affecting other goals adversely. However, in reality, continuous compromises and trade-offs have to be made for a particular design goal as it is almost impossible to decouple the interlinked flow behaviour [11], *i.e.* lift and drag forces and noise emission in the case of the high-lift systems.

Studies have shown that the deformation shape and curvature of the morphing structure significantly affects the aerodynamic performance of the airfoils. Sanders *et al.* [13] conducted investigations on airfoils fitted with conventional flaps and conformal morphing trailing edges. It was found that the conformal morphing trailing edge has some distinct aerodynamic benefits over conventional mechanical flaps and the pressure distribution over the airfoil was found to be dependent on the shape of the deformed control surfaces. Daynes *et al.* [14] showed that a morphing flap can provide the same change in the lift coefficient with a 30% less tip deflection compared to a hinged flap of equal flap length. This enhanced control effectiveness is believed to originate from the differing geometries. Wolff *et al.* [15] conducted a two-dimensional numerical investigation of a wind turbine airfoil fitted with morphing trailing edges and found that the deformed morphing trailing edge significantly affects the lift coefficient and stall behaviour of the airfoil. Results showed that the changes to the lift coefficient are dependent on the size, curvature and deflection angle of the deformed trailing edge and strongly curved deformed trailing edge can produce lower maximum lift-to-drag ratio and also increased the root bending moment coefficient compared to a gently curved deformed trailing edge. Campanile *et al.* [16] developed a belt-rib morphing airfoil concept and proposed a model to study the possible actuation requirement reduction by exploiting the aerodynamic and aeroelastic amplification effects on airfoils. Effects of different deformation modes of morphing airfoil and conventional airfoil using hinged flap were quantitatively evaluated and results show that higher slope at trailing edge of belt-rib airfoil leads to large change in lift. In a more recent study, Ai *et al.* [17, 18] proposed a novel morphing trailing edge design using honeycomb core of axial variable stiffness and proved that introducing variable stiffness materials into the morphing structures could change the actuation energy of the system and also enable the tailoring of the morphing profiles, which significantly affects the aerodynamic and aeroacoustic performance of the airfoils. Yokozeki *et al.* [19] developed a morphing airfoil concept using corrugated structures and wind tunnel tests of the demonstrator showed that the morphing wing presented superior properties in lift coefficient compared to a reference wing using conventional flap, which was believed to result from the seamless morphing deformation.

Even though the progress has been consistent on the structural aspects of morphing over the last decade, detailed understanding and documentation of the aerodynamic and aeroacoustic aspect of morphing technology is lacking. In this paper, detailed experimental and numerical studies have been performed to investigate the effects of morphing profiles on the aerodynamic and aeroacoustic performance of airfoils. A NACA 0012 airfoil is chosen for the tests and fitted with a series of morphing trailing edges having the same flap-tip deflection but with different camber profiles. Wind tunnel tests including aerodynamic forces measurements and wake development analysis are carried out on a

wing model. DES studies are also carried out to further investigate the flow structures, boundary layers, shear stresses, wall-pressure spectra and far-field noise.

II. Experimental and Computational Setup

A. Airfoil Model Setup

RAKU-TOOL® WB-1222 polyurethane board was used to manufacture NACA 0012 airfoil model with a chord length of $c = 0.2$ m and a span length of $l = 0.45$ m. The airfoil was designed to facilitate multiple interchangeable trailing-edge flaps with lenght of $b = 0.06$ m ($0.3c$) and having different morphing camber profiles and deflection angles. Ai *et al.* [17, 18] tested the aerodynamic and aeroacoustic performance of novel morphing flaps using Xfoil-BPM model. The results from the study were then used to design the morphing flap camber profiles (see Fig. 1) used in the current experimental and computational study. The airfoils were tested for morphing flaps with varying camber profiles for the deflection angle of, $\beta = 10°$. A ratio between the morphing flap flap length, b and tip deflection length was used to define the morphing flap tip deflection angle, β. As shown in Fig. 1, Hinged-Flap airfoil represents a flap with typical hinged flap movement and the following Morphed-Flap (1-4) airfoil cases employ a conformal morphing flap profiles with increasing camber.

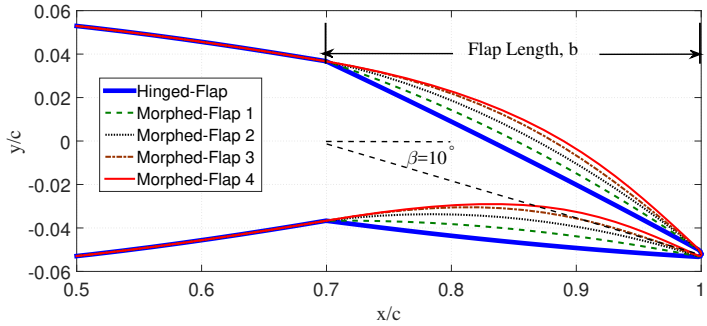

Fig. 1. NACA 0012 airfoil fitted with different morphing flaps with deflection angle of β=10°.

B. Wind Tunnel and Experimental Setup

Aerodynamic force measurements and wake development of a NACA 0012 airfoil fitted with morphing flaps having various camber profiles have been experimentally tested at the University of Bristol wind tunnel facilities; (i) low speed closed-circuit wind tunnel that has an octagonal working area of 2.1 m × 1.5 m × 2 m, with a contraction ratio of 3:1 and a stable working velocity range of 10 m/s to 60 m/s and (ii) open jet wind tunnel with diameter of 1.1 m, with a maximum reliable speed of 30 m/s and minimum turbulence level of 0.05%; (iii) low turbulence closed-circuit wind tunnel with an octagonal working section of 0.8 m × 0.6 m × 1 m, contraction ratio of 12:1, maximum velocity of 100 m/s and with turbulence level as low as 0.05%.

Force measurement setup: An AMTI OR6-7-2000 force platform from Advanced Mechanical Technology Inc., has been used to measure the aerodynamic forces for the NACA 0012 airfoil cases. The lift (L) and drag (D) forces were measured in the large low speed wind-tunnel where the blockage effects were found to be negligible. Two circular side-plates with a radius of 0.17 m were used to reduce the three dimensionality effects of the flow around the airfoil. The data collected for a period of 30 s with a sampling frequency of 37 Hz.

Wake measurement setup: Hot-wire measurements were made at six different streamwise locations in the wake of NACA 0012 airfoil with morphing-trailing-edges. Dantec 55P16 single hot-wire probe was used to measure the steady flow velocities in the wake. The hot-wire probes were calibrated using a Dantec 54H10 two point mode hot-wire calibrator. The data was collected for a time period of 20 s with a sampling frequency of 40 kHz.

Pressure measurement setup: The pressure measurements were made using MicroDaq pressure scanners with full scale accuracy output of up to 0.05%. The measurements were made at 40 pressure ports that were well distributed and flush mounted on the surface of the airfoil. The ports closest to the trailing-edge was at $x/c = 0.9$. The measurements were carried out for a period of 60 s with a sampling frequency of 500 Hz.

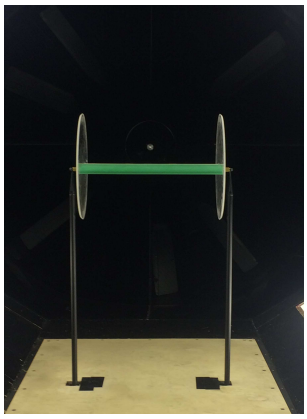

Fig. 2. NACA 0012 airfoil with side-plates set up in the wind tunnel.

C. Computational Setup

DES studies have been carried out to investigate the flow characteristics and understand the noise generation mechanism around the hinged and morphing flaps. Initially, Reynolds-averaged Navier-Stokes (RANS) numerical simulations were performed using OpenFOAM open source code and Spallart-Allmaras ($S-A$) turbulence model. The validated RANS [10] results were then used to initiate the DES simulations using the $S-A$ turbulence model. The three-dimensional multi-block structured C-H type mesh used in the simulations were generated using commercial software ICEM-CFD. After a domain independence study the domain size was set to be 10 c in the streamwise and 5c in the crosswise direction. The domain had a spanwise thickness of 0.1 c. The cell distribution along the airfoil was $L_x \times L_y \times L_z = 260 \times 120 \times 32$. In order to accurately capture the boundary layer the airfoil wall was set to have a $y^+ \approx 0.5-1$ with 40 grid points within $y = 0.035c$ close to the wall. The grid spacing along the streamwise direction corresponds to $x^+ \approx 30$ and is clustered towards the airfoil leading-edge and trailing-edge. To capture the wake behaviour accurately 1.5 c downstream of the trailing-edge was densely populated with 200 grid points. In the spanwise direction, the grid spacing was uniformly distributed corresponding to $z^+ \approx 35$. All the simulations were carried out for 30 flow through times (FTT) and the data was collected for only the last 10 FTT. A CFL value of $C_{max} \leq 1$ was maintained throughout the simulations with a time step of $\Delta t = 2.75 \times 10^{-6}$ s.

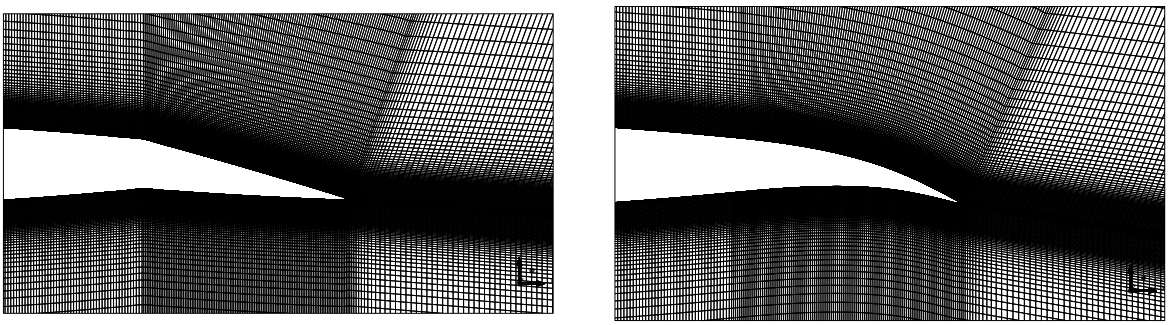

a) Hinged-Flap **b) Morphed-Flap 4**

Fig. 3. NACA 0012 fitted with different morphing flap with a deflection angle of $\beta = 10^\circ$ for the HF and MF-4 airfoil.

III. Results and Discussion

A. Force Measurements

The lift and drag force measurements for NACA 0012 airfoil fitted with five different types of morphing flap profiles (Hinged-Flap to Morphed-Flap 4) with a deflection angle of $\beta = 10°$ at the flow velocity of $U_\infty = 25$ m/s, corresponding to a chord-based Reynolds number of $Re_c = 3.5 \times 10^5$ are presented in Fig. 4. Even though the aerodynamic force measurements were carried out for three different velocities only $U_\infty = 25$ m/s was presented here as the C_L and C_D were found to be independent of Reynolds number for the tested flow velocities.

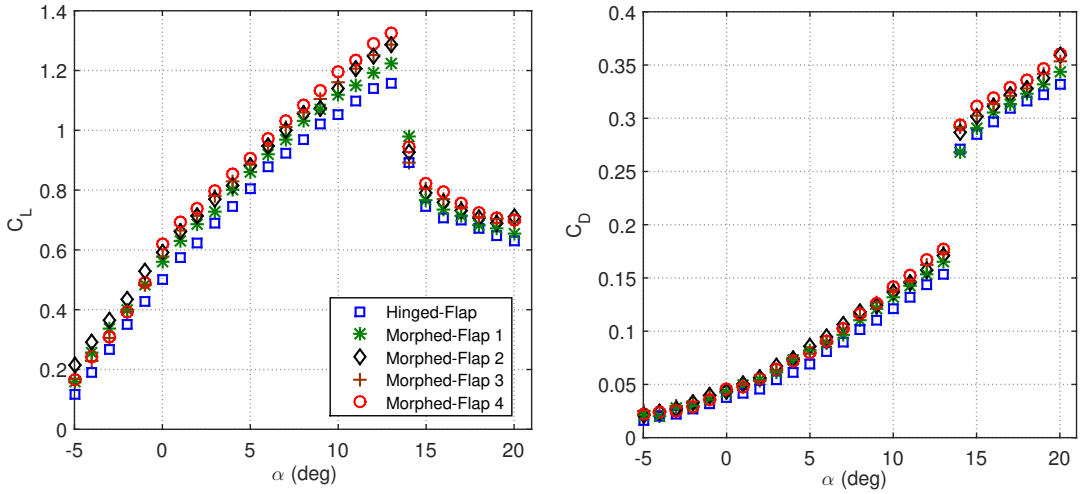

Fig. 4. Lift coefficient results for NACA 0012 airfoil fitted with various morphing flaps of $\beta = 10°$, at the flow velocity of $U_\infty = 25$ m/s ($Re_c = 3.5 \times 10^5$).

The lift and drag results presented in Fig. 4 clearly show that the variation in the morphing flap camber profiles significantly affects the C_L and C_D for the tested angles of attack range. An increase in $C_{L,max}$ of up to 13% can be observed for the highly cambered MF-4 airfoil (Morphed-Flap 4) compared to the simple hinged flap HF airfoil (Hinged-Flap) just before entering stall at $\alpha = 13°$. The C_L for HF airfoil with the hinged flap has the lowest $C_L - \alpha$ curve out of all the tested camber profiles. This will be further discussed in the following section. The highest C_L was observed for the highly cambered MF-4 airfoil for angles of attack ranging from $\alpha = 0°$ to $20°$. However, at negative angles of attack, $\alpha = -5°$ to $0°$, MF-4 airfoil appears to have reduced aerodynamic performance close to that of the MF-2 airfoil. At negative angles of attacks, from $\alpha = -5°$ to $0°$ the highest C_L was achieved by MF-3 airfoil. Figure 4 also shows that at the stall angle of attack ($\alpha = 13°$), the C_D of MF-4 airfoil increases up to 14% relative to that of the HF airfoil. The overall drag performance of the morphing flap cases increases with the increase in flap camber profile. The MF-4 airfoil with the largest morphing flap camber results in the highest C_D compared to the other cases.

Figure 5 shows the lift-to-drag (L/D) ratio results for the HF and MF-4 airfoils. The results clearly show that the overall L/D ratio of HF airfoil is larger than that of the MF-4 airfoil. At negative angles of attack, $\alpha = -2°$ it can be observed that the HF airfoil's L/D is about 25% greater than that of the MF-4 airfoil. However, this large difference between the two cases in L/D gradually decreases as the angle of attack is increased. The L/D difference between the airfoils decreases to 9% at $\alpha = 0°$, 8% at $\alpha = 10°$ and to just 4% at stall angle of $\alpha = 13°$. The polar curves of C_L and C_D shown in Fig. 5 summarises the lift and drag performance between the HF and MF-4 airfoils, showing that the MF-4 airfoil has increased C_L and C_D as the angles of attack increases, especially close to the stall angle. Note, however, that the stall angle was not found to have changed as a result of morphing flap profiles and further studies are necessary for understanding the post-stall properties and flow behaviour. The cases with trailing-edge deflection angle $\beta = 5°$ are not presented here as the difference between the three tested cases were insignificant for in-depth discussion. Results, however suggest that the effect of morphing profile will be ever more important for larger deflection angles (β), which requires further investigation.

B. Pressure Distribution

The pressure distribution results for both the HF and MF-4 airfoils have been presented in Fig. 6 for the angles of attack, $\alpha = 0°$, $2°$, $4°$ and $6°$ at the flow velocity $U_\infty = 20$ m/s. The overall trend of the pressure distribution results

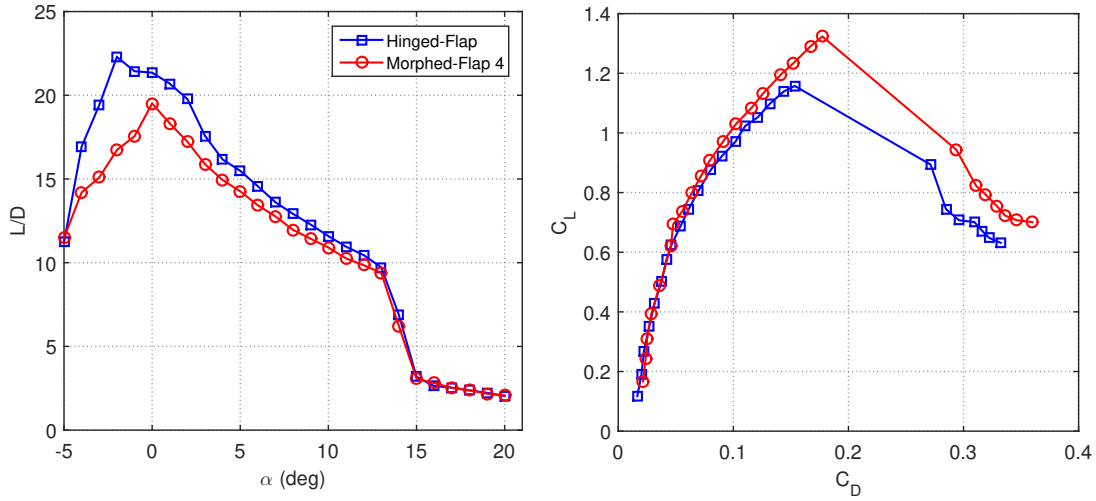

Fig. 5. The lift-to-drag ratio for the Hinged Flap and Morphed Flap 4 airfoils with a deflection angle $\beta = 10°$, at the flow velocity of $U_\infty = 25$ m/s ($Re_c = 3.5 \times 10^5$).

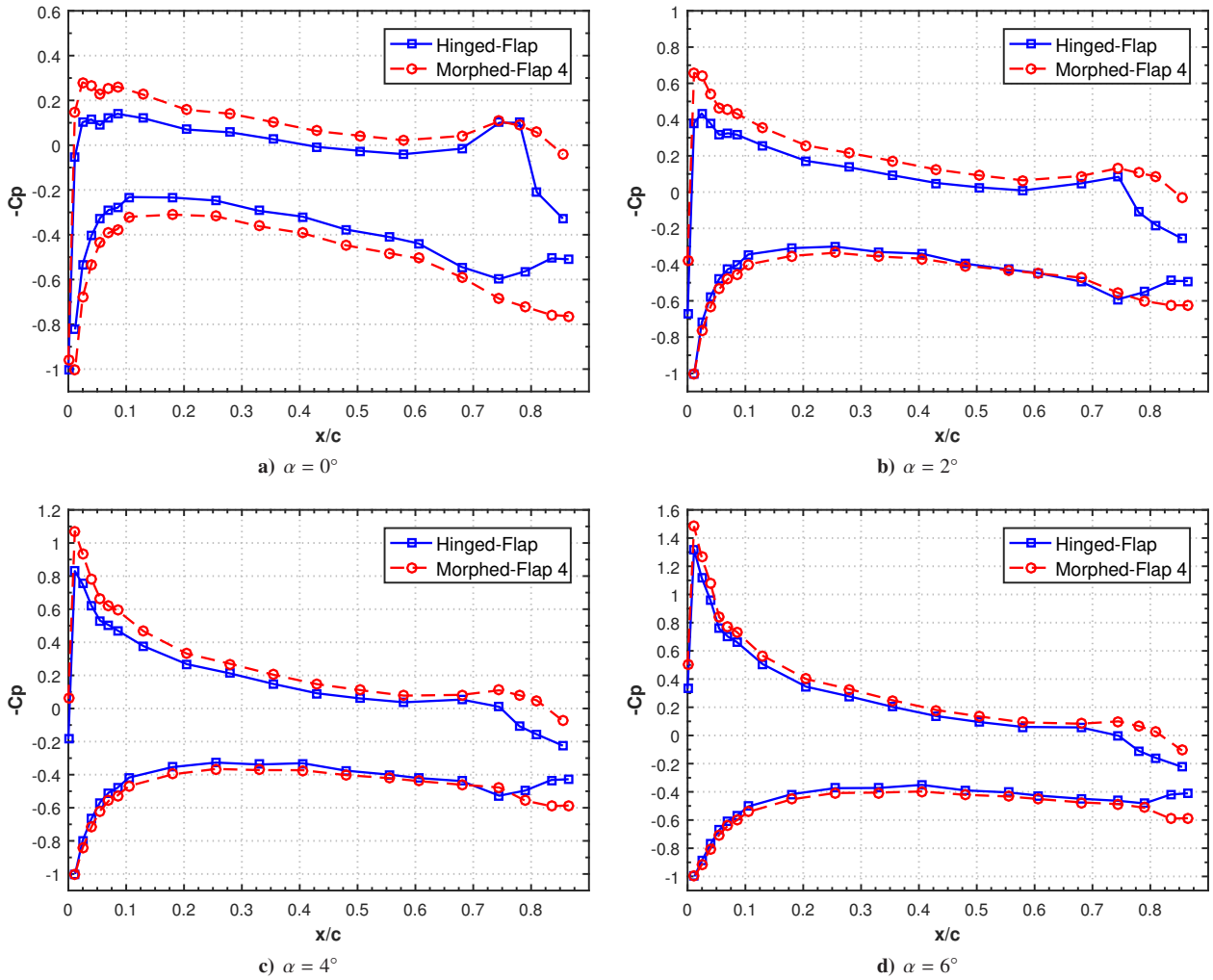

Fig. 6. Pressure coefficient distribution over the Hinged Flap and Morphed Flap 4 airfoils at $U_\infty = 20$ m/s ($Re_c = 2.6 \times 10^5$).

shows a prominent difference between the HF and MF-4 airfoil at low and moderate angles of attack but the relative difference between them subside as the angle of attack is increased. At low angles of attack, $\alpha = 0°$ and 2°, the difference in the C_p suction peak close to the leading edge for HF airfoil is up to 40% lower than that of the MF-4 airfoil. This difference reduces to about 25% and 14% as angles of attack is increased to $\alpha = 4°$ and 6°, respectively and further reduces to about just 7% when the angle of attack is $\alpha = 10°$ (not presented). On the pressure side,a large difference in pressure distribution can be observed only at angle of attack $\alpha = 0°$. However, prominent changes in C_p differences for all the angles of attack can be observed around the flap region with higher differences on the suction-side. These changes in C_p distributions around the flap region are highly dependant on the angle of attack, as shown in Fig. 6. From the presented results it can be seen that even a slight change of camber of the flap with the same deflection angle could substantially change the pressure distribution and the suction peak upstream of the airfoil, especially at low angles of attack.

C. Wake Development

The wake flow field of both the HF and MF-4 airfoil was studied experimentally using hot-wire anemometry. The measurements were carried out at six downstream locations in the mid-span position of the airfoil, $x/c = 1.01$, 1.065, 1.115, 1.125, 1.515 and 2.015 with the leading-edge tip assumed as the datum point as shown in Fig. 7. The tests were performed for angles of attack, $\alpha = 0°$, 2°, 4° and 6° at the flow velocity of $U_\infty = 20$ m/s, corresponding to $Re_c = 2.6 \times 10^5$.

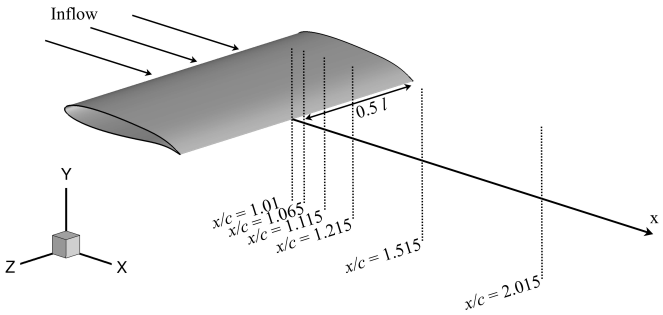

Fig. 7. Airfoil coordinate system along with wake velocity measurements locations.

The velocity profiles for all the tested four angles of attack are presented in Fig. 8. The velocity profiles for $\alpha = 0°$ and 2° at the near-wake location $x/c = 1.01$ show a thicker boundary layer for the MF-4 airfoil relative to the HF airfoil. The overall results for all the presented angles of attack show that at further downstream locations the wake velocity for the MF-4 airfoil has a increased deflection angle compared to the HF-4 airfoil and the level of deflection increases with increasing angle of attack, especially at the far-wake locations $x/c = 1.125$, 1.515 and 2.015. The velocity deficit for MF-4 airfoil appears to have slightly increased relative to the HF airfoil at all the downstream wake locations. The velocity gradient appears to have increased at all angles of attack for the MF-4 airfoil compared to the HF airfoil at the near wake location $x/c = 1.01$.

The measured turbulent kinetic energy (TKE) results from the experimental measurements for HF and MF-4 airfoils at the angles of attack $\alpha = 0°$, 2°, 4° and 6° are presented in Fig. 9. For the angles of attack $\alpha = 0°$ and 2°, at the near-wake location, $x/c = 1.01$ close to the trailing edge, it can be observed that the TKE magnitude for MF-4 airfoil is about 50% higher relative to the HF airfoil on the suction side of the wake profile. The difference between the HF and MF-4 airfoils is up to 60% higher at the location $x/c = 1.065$, for $\alpha = 0°$. This difference in the TKE magnitude between the cases reduces at further downstream locations. At the far-wake locations, $x/c = 1.215$, 1.515 and 2.015, it can be observed that the MF-4 airfoil has a much wider wake towards the pressure surface than that of HF airfoil. From the peak location of the TKE profiles at the far-wake locations, $x/c = 1.215$, 1.515 and 2.015, aforementioned increased deflection angle of MF-4 airfoil can be observed readily. The TKE profiles at angles of attack, $\alpha = 2°$, 4° and 6° for both the tested HF and MF-4 airfoils are presented in Figs. 9c and 9d, respectively. From the results it can be observed that the TKE magnitude has a characteristic double peak behaviour, which was absent at lower angle of attack $\alpha = 0°$. The large difference in TKE magnitude seen between HF and MF-4 airfoils at lower angle of attack $\alpha = 0°$ is not observed here. However, there are still a noticeable differences in TKE magnitude between the cases, with MF-4 airfoil having larger TKE magnitude. The increased deflection of the wake for MF-4 airfoil compared to HF airfoil can also be readily observed for the low and moderate angles of attack at the far-wake

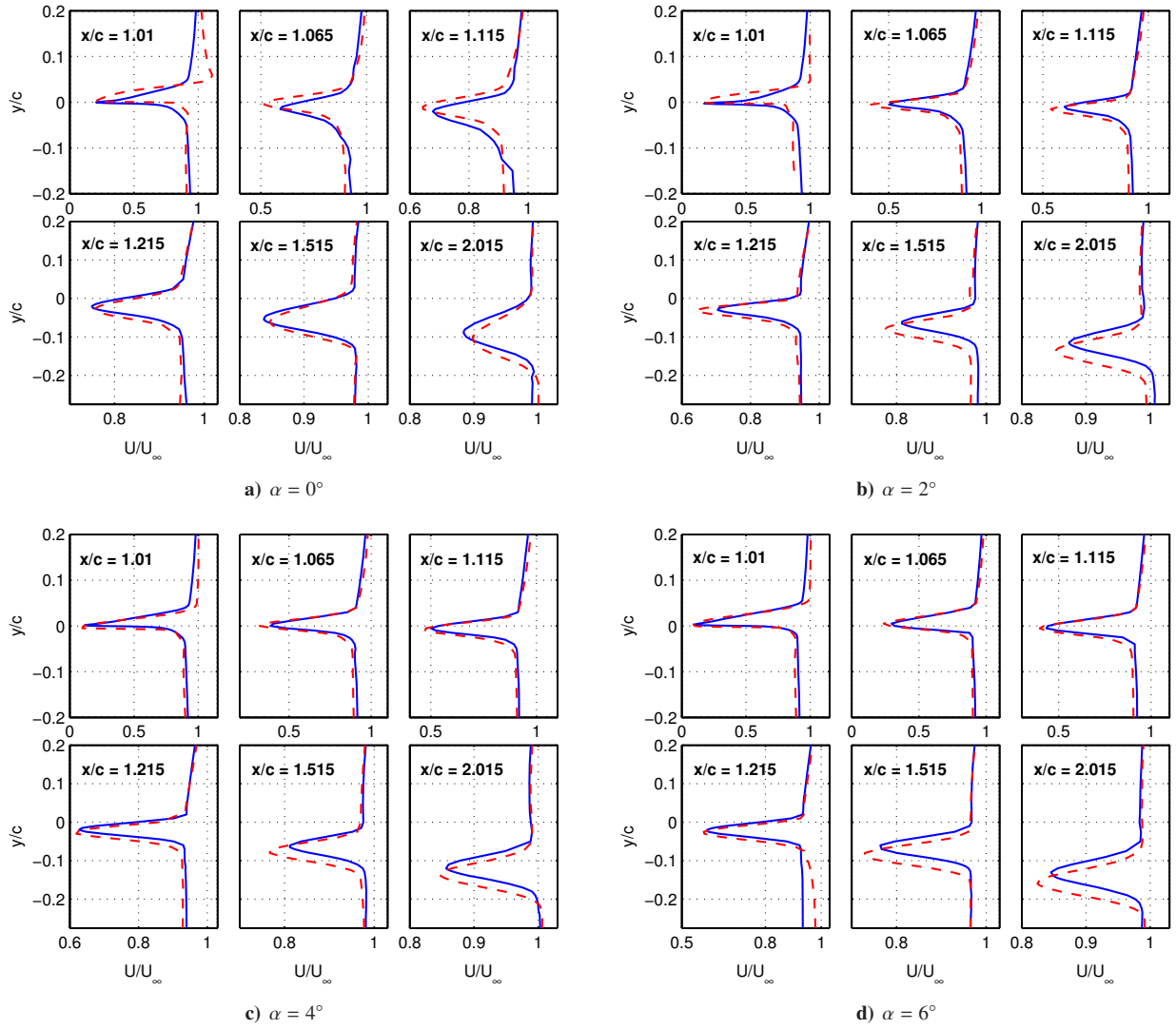

a) $\alpha = 0°$ **b)** $\alpha = 2°$ **c)** $\alpha = 4°$ **d)** $\alpha = 6°$

Fig. 8. Wake velocity profiles at the flow velocity $U_\infty = 20$ m/s, for the Hinged-Flap — and Morphed-Flap 4 - - - airfoils.

the locations, $x/c = 1.215$, 1.515 and 2.015.

1. Wake Flow Structure

DES computational studies for the NACA 0012 airfoil fitted with two morphing flap configurations (HF and MF-4) has been carried out. The simulations were validated with the experimental measurements at the wake region. The validated computational results were used to further investigate the flow behaviour around the airfoil's morphing flap and also to calculate the far-field noise levels using Curle's acoustic analogy. For the purpose of brevity the results presented and discussed here are only for angles of attack, $\alpha = 0°$ and $4°$ at the flow velocity of $U_\infty = 20$ m/s ($Re_c = 2.6 \times 10^5$).

The results of the mean velocity profiles at the wake for the HF and MF-4 airfoils are presented in Fig. 10. It can be observed that the DES S-A model accurately predicts the velocity deficit and dip location at $\alpha = 0°$ compared to the experimental data at the near-wake locations, namely $x/c = 1.01$, 1.065 and 1.115 for the HF airfoil but slightly overpredicts the velocity deficit for the MF-4 airfoil. The mean velocity profiles for both the HF and MF-4 airfoils at $\alpha = 4°$ show very good agreement with the experimental data at $x/c = 1.01$ but slightly underpredicts the velocity deficit further downstream at the locations $x/c = 1.065$ and 1.115. At the far-wake location, $x/c = 2.015$, the S-A model fails to predict the velocity deficit, wake width and the peak location accurately for both the cases. The peak location of the experimental data for both the HF and MF-4 airfoils have a larger flow deflection angle (flow turning

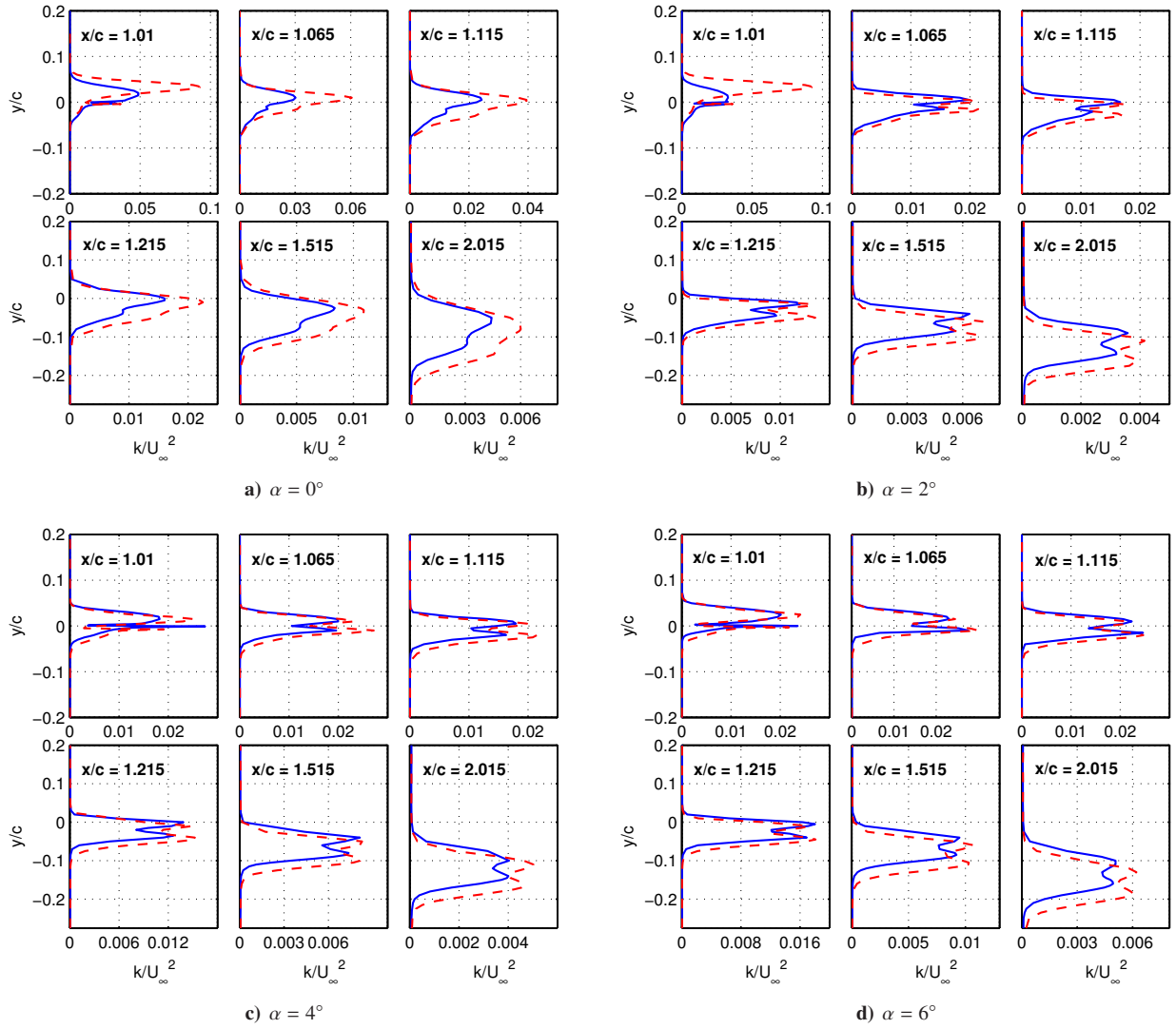

a) $\alpha = 0°$ **b)** $\alpha = 2°$

c) $\alpha = 4°$ **d)** $\alpha = 6°$

Fig. 9. Wake turbulent kinetic energy profiles at the flow velocity $U_\infty = 20$ m/s, for the Hinged-Flap — and Morphed-Flap 4 - - - airfoils.

angle) compared to the S-A model predictions. The S-A model's failure to accurately predict the flow at far-wake locations are mostly due to not incorporating the open-jet wind tunnels effects into the simulation.

The iso-surfaces of the Q-criterion ($Q = 1 \times 10^5 s^{-2}$) with contours of vorticity magnitude for the HF and MF-4 airfoils at the angles of attack $\alpha = 0°$ and $4°$ are shown in Fig. 11. From the iso-surfaces for the angle of attack $\alpha = 0°$ in Fig. 11, it can be observed that for the HF airfoil, the separation on the suction side occurs after the flap hinge ($x/c \approx 0.9$), whereas for the MF-4 airfoil due the smooth cambered profile the flow does not separate on the suction side. For the HF airfoil the separation on the pressure side occurs just after the hinge of the flap ($x/c \approx 0.65$) and reattaches to the surface right after the hinge ($x/c \approx 0.8$) before mixing into the airfoil wake. For the MF-4 airfoil the separation on the pressure side occurs very early ($x/c \approx 0.8$) and reattaches only at the very tip ($x/c \approx 0.95$) of the trailing-edge just before separating and mixing into the airfoil wake. This large separation with unsteady fluctuations on the pressure side between $x/c \approx 0.8$ and $x/c \approx 0.95$ on for the MF-4 airfoil could be the primary reason for the larger wake velocity deficit compared to HF airfoil, as discussed in previous sections. This separation on the pressure side for the MF-4 airfoil also appears to have an influence on the velocity reduction in the nearby surrounding area, which corresponds to the wider wake, increased TKE and increased pressure as discussed earlier.

From the iso-surface plots at $\alpha = 4°$ in Fig. 11 it can be observed that for the HF airfoil case, the separation on the suction side occurs slightly earlier relative to $\alpha = 0°$ case, where the separation on the suction side occurs after the flap hinge point ($x/c \approx 0.8$). However, for the MF-4 airfoil shown in Fig. 11d, the separation on the suction side is much delayed and occurs very close to the trailing-edge ($x/c \approx 0.85$), quite close to the separation location observed at

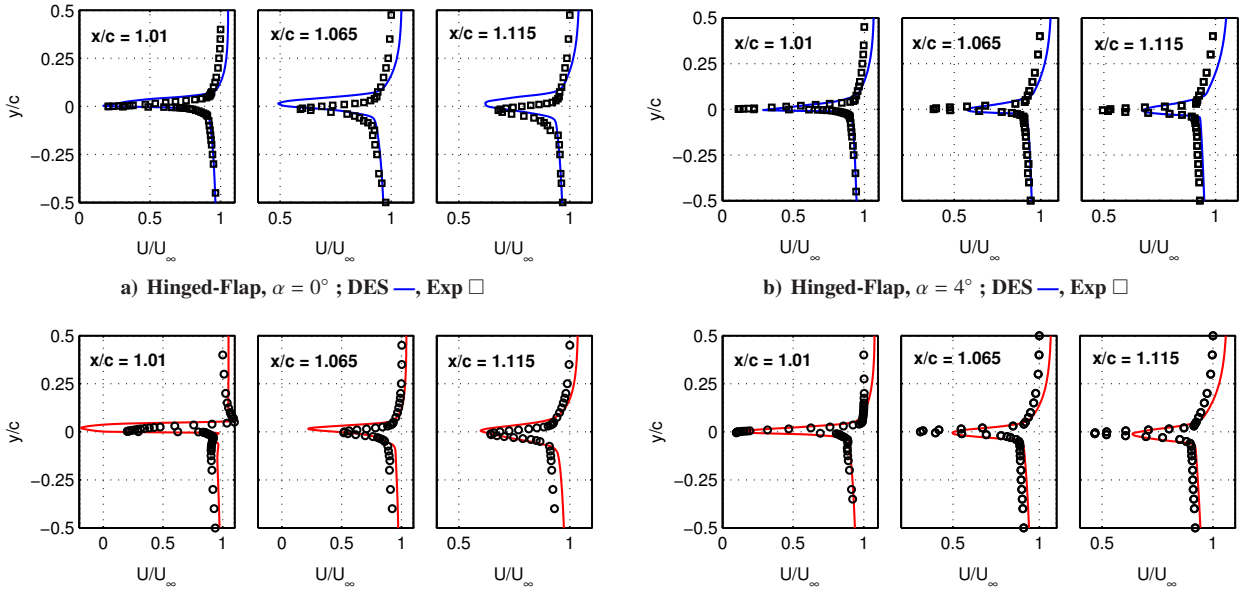

a) Hinged-Flap, $\alpha = 0^\circ$; DES —, Exp □

b) Hinged-Flap, $\alpha = 4^\circ$; DES —, Exp □

c) Morphed-Flap 4, $\alpha = 0^\circ$; DES —, Exp ○

d) Morphed-Flap 4, $\alpha = 4^\circ$; DES —, Exp ○

Fig. 10. Wake velocity profiles of DES simulation along with experimental measurements for the flow velocity of $U_\infty = 20$ m/s.

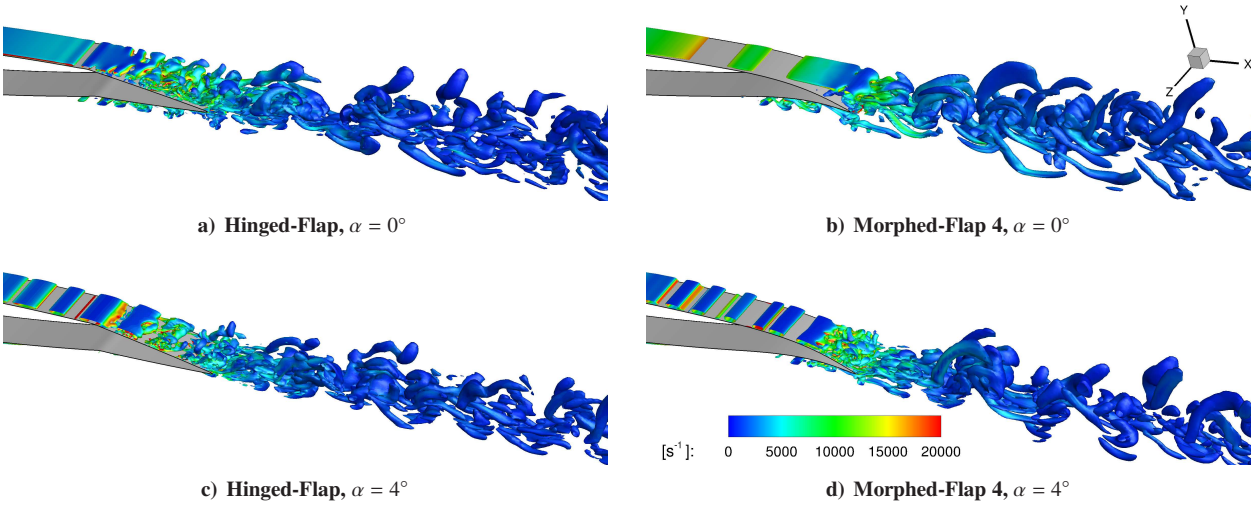

a) Hinged-Flap, $\alpha = 0^\circ$

b) Morphed-Flap 4, $\alpha = 0^\circ$

c) Hinged-Flap, $\alpha = 4^\circ$

d) Morphed-Flap 4, $\alpha = 4^\circ$

Fig. 11. Iso-surfaces of Q-criterion of $Q = 1 \times 10^5 s^{-2}$ for Hinged Flap and Morphed Flap 4 airfoil with contours of vorticity magnitude.

$\alpha = 0^\circ$. For the angle of attack $\alpha = 4^\circ$ the recirculation on the pressure side for HF airfoil was absent, whereas for the MF-4 airfoil the separation occurs at the same location as that of the suction side ($x/c \approx 0.85$) close to the trailing-edge before mixing into the airfoil wake. The onset of this large separation on the pressure side of the MF-4 airfoil appears to be further delayed with increase in angle of attack. The separation for the MF-4 airfoil on the pressure side always appears to be larger than that of the HF airfoil resulting in increased wake velocity deficit and TKE that adds to the increased form drag for the MF-4 airfoil as seen earlier in the force measurements. This large flow separation on the pressure side of the highly cambered trailing-edge profiles can be avoided by the use of independent surface morphing, since the cambered flap results in favourable delayed separation on the suction side but also results in unfavourable recirculation on the pressure side. An optimum design would require a different camber profile for the pressure side to delay the onset of early separation and recirculation on the lower side of the morphing flap. For the HF airfoil and MF-4 airfoil, at $\alpha = 4^\circ$ the boundary layer develops 2-D Tollmien-Schlichting (TS) instability waves that occur as rolled up two-dimensional vortical structures, after an initial stable state. These two-dimensional structures develops into turbulent three-dimensional structures closer to the trailing edge. The two-dimensional fixed vortical structures

are also found on the flap pressure side of the MF-4 airfoil for both presented the angles of attack.

2. *Boundary Layer Measurements*

The boundary layer results from the DES for the tested HF and MF-4 airfoils, at $\alpha = 0°$ and $4°$ are presented in Figs. 12 and 13, respectively. The mean velocity profiles on the airfoil suction side, for $\alpha = 0°$, in Figs. 18h and 18e show very prominent difference between the HF and MF-4 airfoils. For the HF airfoil the boundary layer shows a steady growth between $x/c = 0.65$ and 0.75, after which the velocities change direction at $x/c = 0.85$ and 0.90. The flow then separates at $x/c = 0.95$, which can be determined by the sudden decrease in the velocity gradient ($\delta U/\delta y$). The negative velocities at the locations $x/c = 0.85$ and 0.90 can be attributed to the emergence of the vortices that leads to the boundary layer separation at $x/c = 0.95$ and also leads to energy loss in the flow. The boundary layer profile for the MF-4 airfoil in Fig. 18e shows a steady growth in the boundary layer profile from the location $x/c = 0.65$ to 0.95 with no separation, as previously observed in the iso-contours of Q-criterion in Fig. 11. This is due to the smoother flap curvature that aids in the increased velocity and lower pressure on the suction side of the flap. The larger C_D and the lower L/D for the MF-4 airfoil discussed before can now be attributed to the increased drag from the larger boundary layer with no separation on the suction side of the MF-4 airfoil relative to the HF airfoil. The velocity profile on the suction side of the HF airfoil in Fig. 18f shows a well developed boundary layer with negative velocities at $x/c = 0.65$ and 0.75, indicating a small recirculation area at the flap hinge. A well reattached flow can then be seen at downstream locations $x/c > 0.85$. The flow on the pressure side of the MF-4 airfoil in Fig. 18g shows a much larger boundary layer relative to the HF airfoil at $x/c = 0.65$ and 0.75 with negative velocities at $x/c = 0.75$. The flow appears to be completely separated at $x/c = 0.85$ but reattached at locations $x/c = 0.90$ and 0.95. This observation concurs with the iso-contour Q-criterion results previous discussed where a large area of unsteady separated flow was observed over the flap pressure side of the MF-4 airfoil.

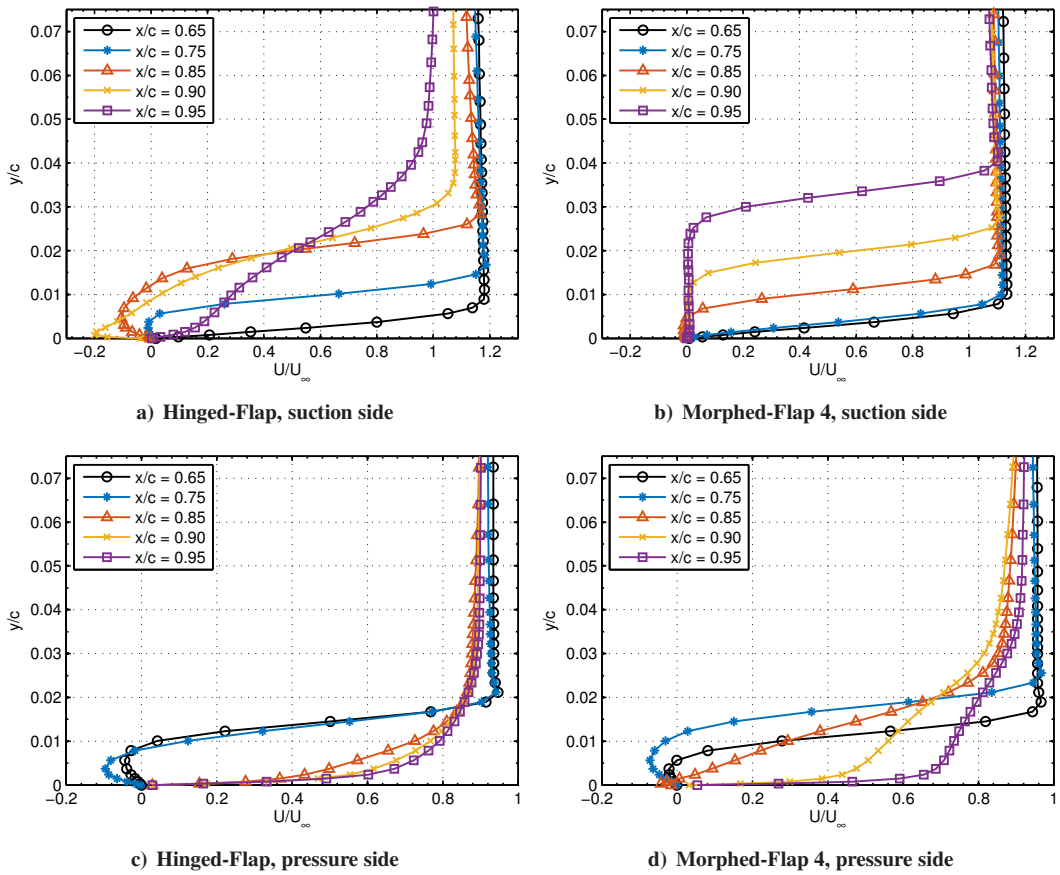

a) Hinged-Flap, suction side

b) Morphed-Flap 4, suction side

c) Hinged-Flap, pressure side

d) Morphed-Flap 4, pressure side

Fig. 12. Boundary layer profiles on the suction and pressure side at various streamwise locations of Hinged Flap and Morphed Flap 4 airfoils at angle of attack $\alpha = 0°$ for flow velocity of $U_\infty = 20$ m/s ($Re_c = 2.6 \times 10^5$).

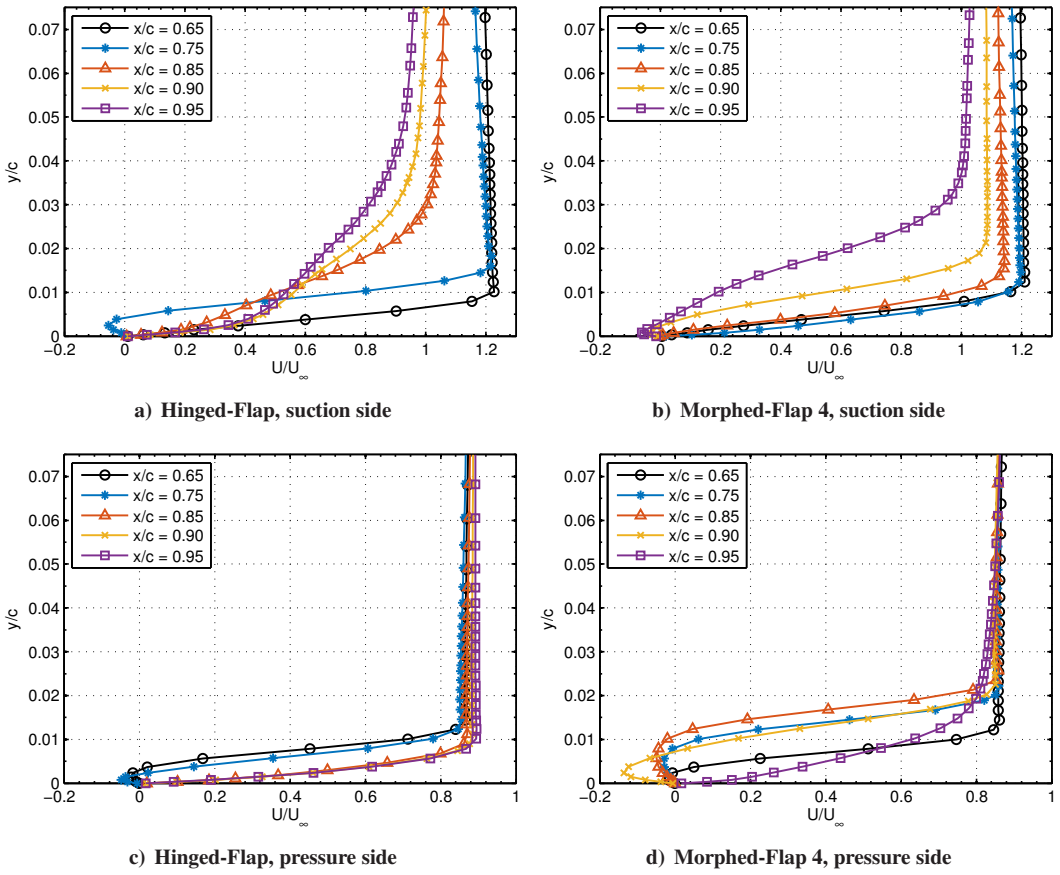

a) Hinged-Flap, suction side

b) Morphed-Flap 4, suction side

c) Hinged-Flap, pressure side

d) Morphed-Flap 4, pressure side

Fig. 13. Boundary layer profiles on the suction and pressure side at various streamwise locations of Hinged Flap and Morphed Flap 4 airfoils at angle of attack $\alpha = 4°$ for flow velocity of $U_\infty = 20$ m/s ($Re_c = 2.6 \times 10^5$).

The boundary layer results on the suction side of the HF and MF-4 airfoils at $\alpha = 4°$ are presented in Figs. 13a and 13b, respectively. For the HF airfoil the flow on the suction side remains attached up to $x/c = 0.75$, after which the flow separates with decreasing velocity gradients at the following downstream locations. For the MF-4 airfoil the boundary layer thickness is smaller relative to that of the HF airfoil at the locations $x/c = 0.65$, 0.75 and 0.85 and the separation occurs at further downstream location of $x/c = 0.90$. The velocity gradient at all locations for the MF-4 airfoil is higher than that of the HF airfoil. This suggests higher shear stress over the surface of the MF-4 airfoil relative to the HF airfoil, which also corresponds with the previously discussed higher drag of the MF-4 airfoil. The flow on the pressure side of both the HF and MF-4 airfoils are presented in Figs. 13c and 13d. The boundary layer for the HF airfoil at $\alpha = 4°$ shows a fully attached flow on the pressure side of the airfoil. However, the MF-4 airfoil at $\alpha = 4°$ shows a much thicker boundary layer with negative velocities at almost all the locations from $x/c = 0.65$ to 0.90, which suggests a large fixed vorticity present on the pressure side of the MF-4 airfoil, as previously seen in the iso-contours.

3. Reynolds Stress Tensors

The two normal components of the Reynolds stresses ($U^2_{RMS}\, V^2_{RMS}$) are shown in Fig. 14 over the flap of HF and MF-4 airfoils. The same colour scale except for Fig. 14d, is used to facilitate comparison of the plots. For the HF airfoil, at $\alpha = 0°$, increased fluctuations can be observed at $x/c = 0.85$, where reversed flow was previously shown in the boundary layer results. The peak values of shear stresses can be seen at about $x/c = 0.95$, where the flow was separated in the boundary layer results discussed above. For MF-4 airfoil the increased values of stresses were observed only at locations aft of the trailing-edge. Two distinct peaks can be observed very close to the trailing edge. The increased shear stresses corresponds to the high TKE observed in the hot-wire measurements in Fig. 9. The increased shear stresses can also be observed on the pressure side of the MF-4 flap from $x/c = 0.8$ onwards, which can be attributed to the recirculation as previously seen in the iso-contours and boundary layer results. The magnitude of the crosswise

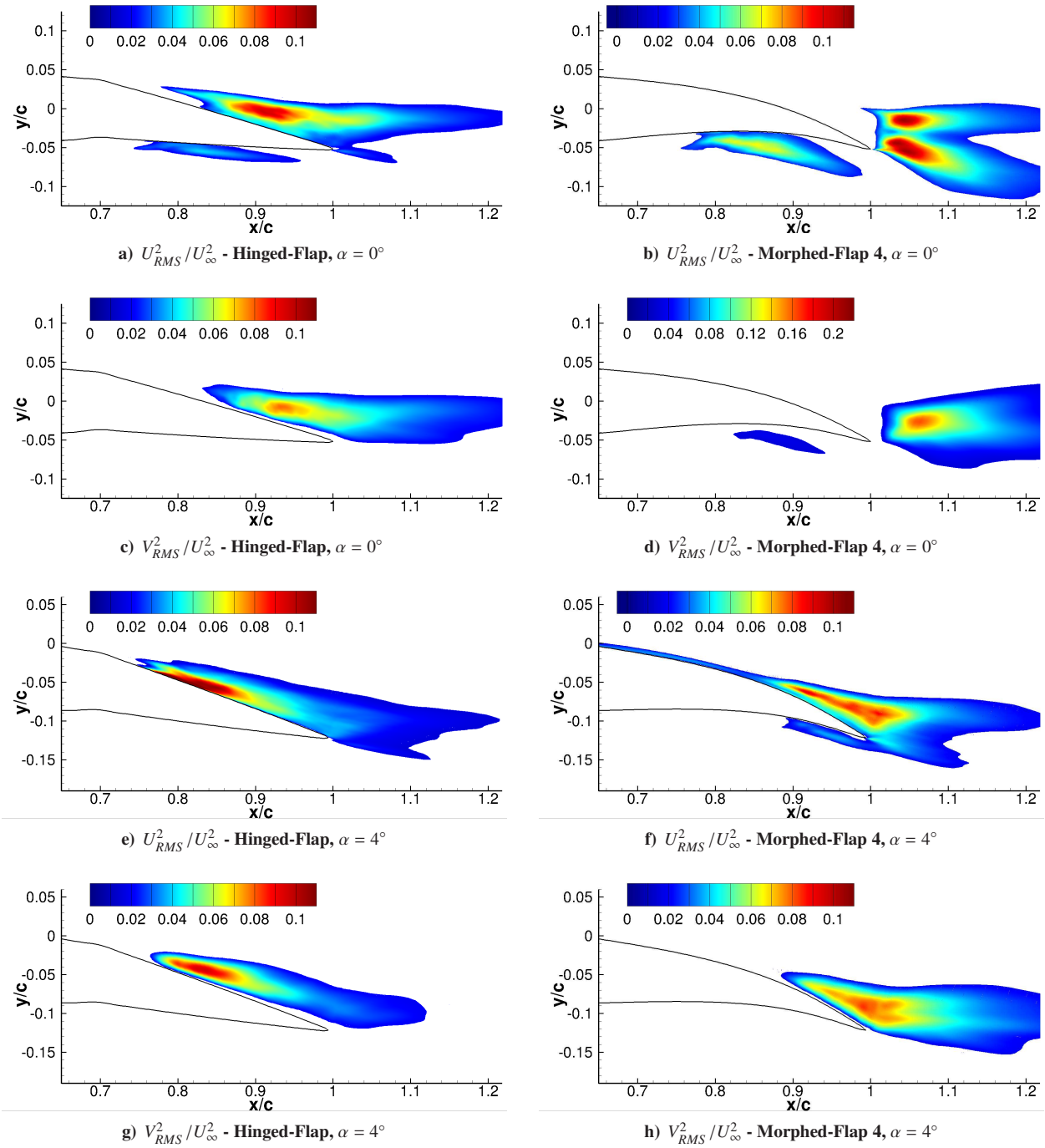

a) U^2_{RMS}/U^2_∞ - **Hinged-Flap,** $\alpha = 0°$

b) U^2_{RMS}/U^2_∞ - **Morphed-Flap 4,** $\alpha = 0°$

c) V^2_{RMS}/U^2_∞ - **Hinged-Flap,** $\alpha = 0°$

d) V^2_{RMS}/U^2_∞ - **Morphed-Flap 4,** $\alpha = 0°$

e) U^2_{RMS}/U^2_∞ - **Hinged-Flap,** $\alpha = 4°$

f) U^2_{RMS}/U^2_∞ - **Morphed-Flap 4,** $\alpha = 4°$

g) V^2_{RMS}/U^2_∞ - **Hinged-Flap,** $\alpha = 4°$

h) V^2_{RMS}/U^2_∞ - **Morphed-Flap 4,** $\alpha = 4°$

Fig. 14. Streamwise and crosswise Reynolds stress distribution for the Hinged Flap and Morphed Flap 4 airfoils.

shear stress (V^2_{RMS} component) for the MF-4 airfoil in the wake at $\alpha = 0°$ is highest compared to all the cases. This might be due to the large pressure differences at the trailing-edge caused by mixing of the attached high velocity flow from the suction side with the low velocity flow (due to recirculation) from the pressure side resulting in increased velocity fluctuations with wake shedding aft of the trailing-edge point. The Reynolds stresses at $\alpha = 4°$ for both the HF and MF-4 arifoils are localised on the suction side of the flap. HF airfoil shows elongated increased fluctuation regions extending from $x/c = 0.75$ until the trailing-edge. Whereas the MF-4 airfoil shows a much thicker fluctuations region starting from $x/c = 0.85$ and extending well into the wake region.

D. Aeroacoustic Results

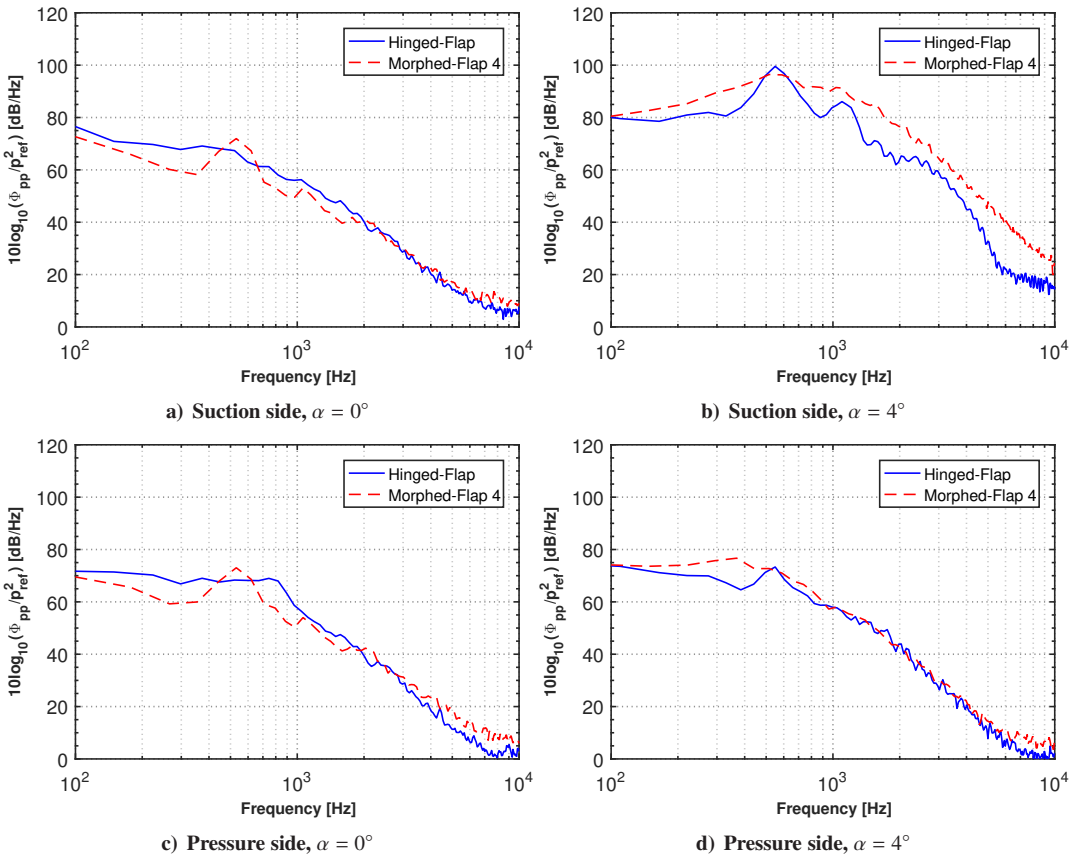

a) **Suction side,** $\alpha = 0°$ b) **Suction side,** $\alpha = 4°$

c) **Pressure side,** $\alpha = 0°$ d) **Pressure side,** $\alpha = 4°$

Fig. 15. Suction and pressure side wall-pressure spectra with reference to 2×10^5 **Pa, at the location** $x = 0.75c$ **for Hinged Flap and Morphed Flap 4 airfoils at angles of attack** $\alpha = 0°$ **and** $4°$**.**

The power spectral density Φ_{pp} of the surface pressure on the suction and pressure sides for the HF and MF-4 airfoils at angles of attack $\alpha = 0°$ and $4°$ are presented in Figs. 15 and 16. The results are presented for two important streamwise location, at $x/c = 0.75$ in a region with attached flow and at $x/c = 0.95$ in a region with separated flow very close to the trailing-edge at mid-span. The wall-pressure spectra at the selected locations are important for far-field noise prediction as they are the input parameters for Curle's analogy used here. For $\alpha = 0°$, at $x/c = 0.75$ (see Fig. 15) on the pressure side a narrowband peak at frequency $f \approx 500$ Hz can be observed only for the MF-4 airfoil. The overall spectral level is lower for the MF-4 airfoil compared to the HF airfoil. For $\alpha = 4°$ on both the pressure and suction side, the wall-pressure spectral levels are lower for the HF-4 but it exhibits a narrowband component, which is absent in MF-4 airfoil. These narrowband peaks observed at both the angles of attack are developed due to boundary layer instabilities, which has been characterised experimentally by Arbey & Batallie [20], showed using DNS by Desqunes et al [21] and also using LES by Winkler *et al* [22]. These discrete narrowband peaks are seen before the flow separates depending on the flap type and angle of attack. These peaks also corresponds with the two-dimensional vortical structures seen earlier in the iso-contours. The wall-pressure spectra results for both the airfoils presented in Fig. 16 at $x/c = 0.95$ show a broadband behaviour on the suction side since the flow is fully turbulent. For the HF airfoil at $\alpha = 0°$, the spectra is up to 25 dB higher than that of the MF-4 airfoil for the entire frequency range. This increase corresponds to the turbulent separated flow previously shown along with the iso-contour and boundary layer result. But, for $\alpha = 4°$ the MF-4 airfoil is up to 12 dB higher relative to the HF airfoil at the low frequency range ($f \leq 450$ Hz) and with minimal difference in the rest of the higher frequency range. This similarity between the cases can be attributed to the separated flow for both the cases at the location $x/c = 0.95$. The pressure side spectrum shows that the MF-4 airfoil has higher spectral levels relative to HF airfoil for both the presented angles of attack $\alpha = 0°$ and $4°$. For the MF-4 airfoil at $\alpha = 0°$ an increase of up to 7 dB can be observed especially at the frequencies higher than $f = 1$ kHz, whereas for $\alpha = 4°$ an increase of up to 16 dB can be observer for the entire presented frequency range compared to that of the HF airfoil. This increased spectral levels for the MF-4 airfoil are

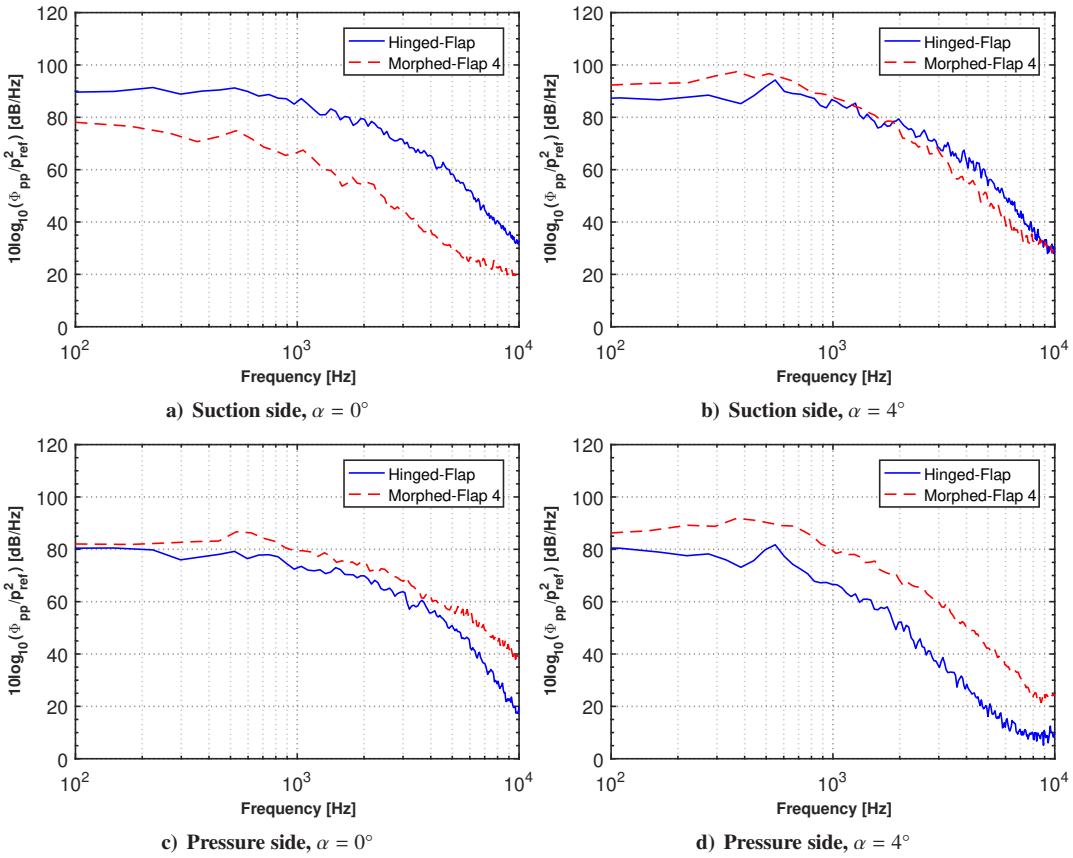

a) Suction side, $\alpha = 0°$ **b) Suction side, $\alpha = 4°$**

c) Pressure side, $\alpha = 0°$ **d) Pressure side, $\alpha = 4°$**

Fig. 16. Suction and pressure side wall-pressure spectra with reference to 2×10^5 Pa, at the location $x = 0.95c$ for Hinged Flap and Morphed Flap 4 airfoils at angles of attack $\alpha = 0°$ and $4°$.

due to the high levels of turbulence and recirculation on the pressure side of the flap region, as shown in the preceding observations of iso-contour and boundary layer development in Sec. III.C.1 and III.C.2.

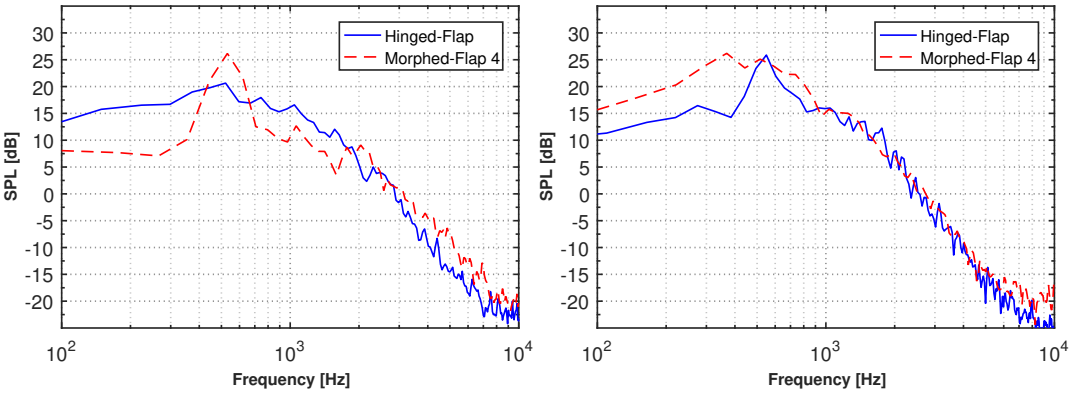

a) $\alpha = 0°$ **b) $\alpha = 4°$**

Fig. 17. Acoustic prediction using Curle's analogy, sound pressure level in dB reference to 2×10^5 Pa, at the location 1.2 m above the trailing-edge for Hinged Flap and Morphed Flap 4 airfoils at angles of attack $\alpha = 0°$ and $4°$.

Trailing-edge noise computations were performed using Curle's acoustic analogy [23]. The source terms for the Curle's analogy are the surface pressure fluctuations acquired at every time step of the DES simulations. The far-field noise calculations were made at 1.2 m above the trailing edge of both the airfoils and the sound pressure level results in reference to P_{ref} are presented in Fig. 17. The results at $\alpha = 0°$ show that the sound level for the MF-4 airfoil are up to 10 dB lower than the HF airfoil below $f < 2$ kHz. However, the MF-4 airfoil exhibits a discrete narrowband peak that

dominates the low frequency range between $f = 400$ and 700 Hz. This shows us that tones produced by the boundary layer instabilities (see Fig. 15) dominate the sound produced by the MF-4 airfoil even though it shows broadband noise reduction in the low-mid frequency range. For $\alpha = 4°$, the MF-4 is free of any tonal components but overall, the broadband noise is higher for the MF-4 airfoil compared to the HF airfoil. The HF airfoil exibits a narrowband peak at low frequency range this can be attributed to the boundary layer instabilities seen in the iso-contours and wall-pressure spectra.

The directivity plots at a distance of $20c$ from airfoil trailing edge for different Helmholtz numbers ($kc = 2\pi f/c_0$) are presented in Fig. 18. The measurements were made at 73 locations around the airfoil trailing-edge at mid-span and the results are normalised with the distance of the measurement point and the airfoil chord length. The acoustic far-field results show that for $kc = 1, 1.5$ and 5 the noise from the HF airfoil is higher at $\alpha = 0°$ and the MF-4 airfoil dominates at $\alpha = 4°$. This shows that as the angle of attack increases the noise level increases along with increased lift from the MF-4 airfoil. This correlates with the previous experimental studies [1], which showed that noise is a strong function of C_L and it increases with C_L, especially after $C_L = 0.5$. The results alternate only at $kc = 2$ where the MF-4 noise levels are higher at $\alpha = 0°$ and the HF airfoil noise levels are higher at $\alpha = 4°$, this is specific for $kc = 2$, corresponding to a frequency of $f = 540$ Hz, where the narrowband peaks are dominant.

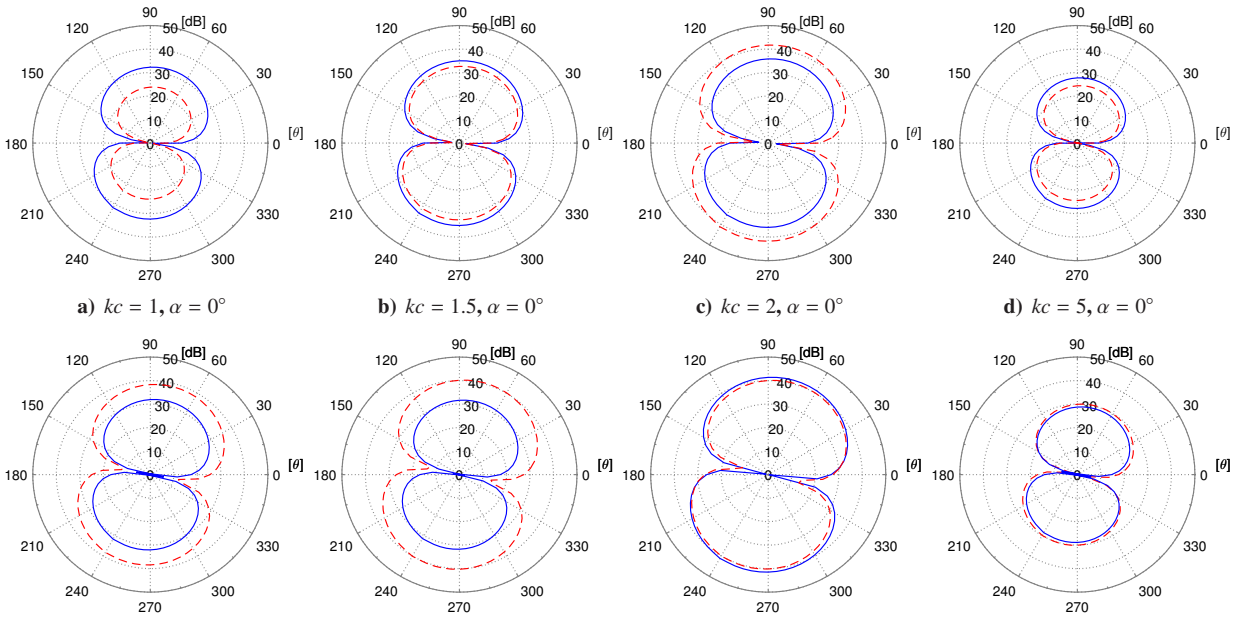

a) $kc = 1, \alpha = 0°$ **b)** $kc = 1.5, \alpha = 0°$ **c)** $kc = 2, \alpha = 0°$ **d)** $kc = 5, \alpha = 0°$

e) $kc = 1, \alpha = 4°$ **f)** $kc = 1.5, \alpha = 4°$ **g)** $kc = 2, \alpha = 4°$ **h)** $kc = 5, \alpha = 4°$

Fig. 18. Acoustic directivity for observer locations at $r = 20c$ for Hinged-Flap — and Morphed-Flap 4 - - - airfoils at angles of attack $\alpha = 0°$ and $4°$.

IV. Conclusion

The aerodynamic and aeroacoustic performance of NACA 0012 airfoil fitted with hinged- and morphed-flap of various camber profiles have been investigated using experimental and numerical techniques. The airfoil was tested for a flow velocity of $U_\infty = 20$ m/s, corresponding to a chord-based $Re_c = 2.6 \times 10^5$. The aerodynamic force measurements have shown that the morphing flap with highly cambered profile (MF-4 airfoil) produces higher lift than that of simple hinged flap profile (HF airfoil). Eventhough higher C_L was observed for the MF-4 airfoil, it came at the cost of increased drag, which reduced the L/D performances upto 9%, especially at low angles of attack. Flow measurements using hot-wire anemometry have been carried out to better understand the aerodynamic characteristics of the morphed flap compared to the hinged flap. The results showed that the turbulent pressure fluctuations and the turbulent kinetic energy in the upper surface also increases along with C_L. A detailed DES study has also been carried out for $\alpha = 0°$ and $4°$ to visualise the flow structure and study the boundary layer, shear stresses, unsteady surface pressure and far-field noise for both of the cases. From these results, it was concluded that the increased drag at low angles of attack is due to the attached boundary layer on the suction side of the MF-4 airfoil. The increased drag can also be attributed to the increased unsteady flow behaviour observed on the pressure side of the MF-4 airfoil that was absent in the HF airfoil. The wall-pressure spectral levels were dominated by narrowband peaks at upstream locations $x/c = 0.75$ that

exists due to the boundary layer instabilities. The downstream locations ($x/c = 0.95$) were free of these peaks and the spectral levels were purely of broadband nature. The far-field noise calculated using Curle's analogy showed decreased noise level for the MF-4 airfoil at $\alpha = 0°$ and increased noise levels for the MF-4 airfoil at $\alpha = 4°$. The narrowband peaks were also distinctly seen in the far-field measurements. High levels of progress on the morphing materials front has been achieved over the past decade but the aerodynamic and aero-acoustic performances of morphing structures have not yet been completely documented. This study shows just the change in the camber profile of the flap with the same deflection angles can have significant impact on the aerodynamic and aeroacoustic behaviour of airfoils at tested Reynolds number. This study also gives an insight into how morphing structures can be optimised to have independent surface morphing of the suction and pressure sides to deliver maximum aerodynamic performances.

References

[1] Lockard, D.P., and Lilley, G.M., *The Airframe Noise Reduction Challenge*, 2004, NASA-TM-2004-213013.

[2] Wagner S., Bareriss R., and Guidati G. *Wind Turbine Noise*, Springer: Berlin, 1996, pp:67-92.

[3] Liu, X., Azarpeyvand, M., and Theunissen, R., "On the Aerodynamic Performance of Serrated airfoils", 22nd International Congress on Sound and Vibration, Florence, Italy, 2015.

[4] Liu, X., Kamliya Jawahar, H., Azarpeyvand, M., and Theunissen, R., "Aerodynamic and Aeroacoustic Performance of Serrated airfoils", AIAA 2015-2201, 2015.

[5] Liu, X., Kamliya Jawahar, H., Azarpeyvand, M., and Theunissen, R., "Wake Development of airfoils with Serrated Trailing Edges", AIAA 2016-2817, 2016.

[6] Lyu, B., Azarpeyvand, M., and Sinayoko, S., "Prediction of noise from serrated trailing-edges", *Journal of Fluid Mechanics*, Vol. 793, pp:556-588, 2016.

[7] Liu, H.R., Azarpeyvand, M., Wei, J.J., and Qu, Z.G., "Tandem cylinder aerodynamic sound control using porous coating", *Journal of Sound and Vibration*, Vol. 334, pp:190-201, 2015.

[8] Showkat Ali, S. A., Liu, X., and Azarpeyvand, M., "Bluff Body Flow and Noise Control Using Porous Media", AIAA 2016-2754, 2016.

[9] Showkat Ali, S. A., Szoke, M., Azarpeyvand, M., and Ilario, C., "Trailing-edge Bluntness Flow and Noise Control Using Porous Treatments", AIAA 2016-2832, 2016.

[10] Ai, Q., Kamliya Jawahar, H., and Azarpeyvand, M., "Experimental investigation of aerodynamic performance of airfoils fitted with morphing trailing-edges", AIAA 2016-1563, 2016.

[11] Gad-el-Hak, M. *Flow Control: Passive, Active, and Reactive Flow Management*; Cambridge University Press: New York, 2006.

[12] Brand. C.B., and Seume, J.R. Flaps for wind turbine applications: results of an acoustic study. *The European Wind Energy Association 2015 Annual Event*, Paris, France, Nov 2015.

[13] Sanders, B., Eastep, F.F., and Froster, E. "Aerodynamic and Aeroelastic Characteristics of Wings with Conformal Control Surfaces for Morphing Aircraft", *Journal of Aircraft*, Vol. 40, No. 1, pp: 94-99, January 2003.

[14] Daynes, S., and Weaver, M.P., "A Morphing Trailing Edge Device for a Wind Turbine", *Journal of Intelligent Material Systems and Structures*, Vol. 23, No. 6, pp: 691-701, March 2012.

[15] Wolff, T., Ernst, B., and Seume, J.R., "Aerodynamic Behaviour of an Airfoil with Morphing Trailing Edge for Wind Turbine Application", *The Science of Making Torque from Wind 2014*, June 2014.

[16] Campanile, L.F., and Anders, S., "Aerodynamic and Aeroelastic Amplification in Adaptive Belt-rib Airfoils", *Aerospace Science and Technology*, Vol. 9, pp:55-63, September 2004.

[17] Ai, Q., Azarpeyvand, M., Lachenal, X., and Weaver, P., "Aerodynamic and Aeroacoustic Performance of Airfoils Using Morphing Structures", *Wind Energy*, Vol. 19, No. 7, pp:1325-1339, July 2016.

[18] Ai, Q., Azarpeyvand, M., Lachenal, X., and Weaver, P., "Airfoil Noise Reduction Using Morphing Trailing Edge", *The 21st International Congress on Sound and Vibration*, Beijing, China., July 2014.

[19] Yokozeki, T., Sugiura,A., and Hirano,Y. "Development of Variable Camber Morphing Airfoil Using Corrugated Structure", *Journal of Aircraft*, Vol. 51, No. 3, pp:1023-1029, May 2014.

[20] Arbey, H., and J. Bataille. "Noise generated by airfoil profiles placed in a uniform laminar flow." *Journal of Fluid Mechanics*, Vol. 134, pp: 33-47, 1983.

[21] Desquesnes, G., M. Terracol, and P. Sagaut. "Numerical investigation of the tone noise mechanism over laminar airfoils", *Journal of Fluid Mechanics*, Vol. 591, pp: 155-182, 2007.

[22] Winkler, Julian, Stphane Moreau, and Thomas Carolus. "Airfoil trailing-edge blowing: Broadband noise prediction from large-eddy simulation." *AIAA journal*, Vol. 50, No.2, pp: 294-303, 2012.

[23] Curle, N. "The influence of solid boundaries upon aerodynamic sound." *Proceedings of the Royal Society of London* Vol. 231. No. 1187, pp: 505514, 1955.